ICICLE: A Model for Glaciated & Mixed Phase Icing for Application to Aircraft Engines

Author, co-author (Do NOT enter this information. It will be pulled from participant tab in MyTechZone)

Affiliation (Do NOT enter this information. It will be pulled from participant tab in MyTechZone)

Abstract

High altitude ice crystals can pose a threat to aircraft engine compression and combustion systems. Cases of engine damage, surge and rollback have been recorded in recent years, believed due to ice crystals partially melting and accreting on static surfaces (stators, endwalls and ducting). The increased awareness and understanding of this phenomenon has resulted in the extension of icing certification requirements to include glaciated and mixed phase conditions. Developing semi-empirical models is a cost effective way of enabling certification, and providing simple design rules for next generation engines. A comprehensive ice crystal icing model is presented in this paper, the Ice Crystal Icing ComputationaL Environment (ICICLE). It is modular in design, comprising a baseline code consisting of an axisymmetric or 2D planar flowfield solution, Lagrangian particle tracking, air-particle heat transfer and phase change, and surface interactions (bouncing, fragmentation, sticking). In addition, an efficient particle tracking method has been developed into the code, which employs the representative particle size distribution at each injection location and a deterministic particle sticking method by using an in-situ particle based scaling factor without aborting the particle trajectories. Various time integration algorithms, including implicit and explicit Euler and Runge-Kutta methods, are discussed and the effect on an acceptable timestep investigated. The model then improves on those available in the literature in three ways: firstly, an adaptation of the Extended Messinger Model (EMM) to mixed phase conditions is incorporated, improving the fidelity of the ice accretion prediction compared with the classical Messinger model. Secondly, an experimentally-derived model for sticking efficiency improves the accuracy of the continuity equation in the EMM; thirdly a simple model for integrating two-way coupling of mass and energy is proposed.

Introduction

There have been numerous cases in recent history of aircraft engine incidents (damage, surge and rollback) whilst flying in conditions associated with high ice water content (IWC). These conditions are typically found (though not exclusively) above the tropics, where convective weather systems loft large moisture concentrations to high altitudes, resulting in condensation and glaciation. At some intermediate altitudes (below ~22,000 ft), ice crystals may coexist with supercooled water, resulting in mixed phase conditions. It is believed that in glaciated or mixed phase conditions, ice crystals enter the engine core compression system, where heat exchange with the warm airflow and engine surfaces results in partial melting. Within a certain range of melt ratios, where particles are sufficiently ‘sticky’, ice accretion can occur. The resulting aerodynamic blockage may result in rollback, or subsequent shedding of accretions may result in blade damage, surge and/or flameout.

The Engine Harmonization Working Group (EHWG) classified 62 turbofan powerloss events since 1990 that were attributed to ice crystal accretion [1]. Of the icing events reviewed by the EHWG, many occurred at altitude in excess of 22,000 ft, the recognised upper limit at which water can exist in liquid form. Up to this point, ice crystals or conglomerates (e.g. snowflakes) were generally viewed as benign to aircraft and engine surfaces. In 2005, the EHWG presented a new interim certification envelope, based on previous ice crystal incidents, which was subsequently adopted by regulatory authorities. As a result, there has been significant effort in recent years to develop semi-empirical models of ice crystal accretion. These models may serve as a cost effective and near-term route to certification (compared with flight tests and sea-level test facilities) and also as preliminary design tools.

Early efforts to adapt existing icing codes to glaciated and mixed phase conditions include Mazzawy [2], an adaptation to NASA Glenn’s icing code GlennICE by Wright et al [3], and a Eulerian approach incorporated in FENSAP-ICE by Nilamdeen and Habashi [4]. Due to a dearth of experimental data on many complex phenomena (mechanical, thermal and multiphase interactions), these models have necessarily included many simplifying assumptions.

More recently, as part of the High Altitude Ice Crystal (HAIC) program, ONERA, the French Aerospace Laboratory, developed a comprehensive 2D model for ice crystal icing, as described in [5], [6]. Particles are treated in the Lagrangian framework, and are allowed to be non-spherical – introducing the need for non-spherical correlations of Nusselt number, Sherwood number and drag coefficient. Particle - surface heat transfer for bouncing or fragmenting impacts is neglected, which is likely to lead to an under-prediction of particle melt ratio. The model uses the Messinger model for liquid water icing [7], with the energy and continuity equations extended to include ice crystals. However, unlike the Extended Messinger Model (EMM) of Myers [8], the Messinger model cannot account for heat transfer through the ice layer or a transient temperature response in the substrate. A semi-empirical erosion model, based on normal and tangential velocity, ice concentration, particle diameter and surface energy is also presented. The model has been tuned and validated against 2D accretion profiles from a number of fundamental experiments ([9]–[11]) in external flows.

Grift et al [12] used Lagrangian particle tracking within an Euler steady flow solver to demonstrate particle tracking and phase change within rotating turbomachinery. This did not, however, include surface interactions (heat transfer, bounce, shatter or stick) or a surface energy balance method (such as the EMM). The use of Eulerian particle tracking was investigated by Iuliano et al [13], where various drag and Nusselt number correlations from the open literature were investigated using three Eulerian-Eulerian codes, from CIRA, ONERA and the University of Twente.

At the University of Oxford, a new comprehensive numerical model has been developed, the Ice Crystal Icing ComputationaL Environment (ICICLE). A Lagrangian particle tracking scheme, with correlations for non-spherical particle Nusselt number, Sherwood number and drag

coefficient, has been written as a baseline model. Phase change is incorporated using Hauk's model for ice crystal melting [14].

The following novel elements are then incorporated into the baseline model:

1) Incorporation of an adaptation to the Extended Messinger Model (EMM) for use in glaciated and mixed phase conditions;
2) Improvements in sticking efficiency and erosion calculation using data from an experimental campaign in an ice crystal icing wind tunnel to calibrate and validate continuity equations;
3) Incorporation of a simple model for two-way coupling of mass and energy.

Code Structure

Physics-based models for the accretion of ice on aircraft surfaces have existed since the 1970s [15]. Models were primarily developed to predict icing on aircraft wings, rotorcraft blades and nacelles when in supercooled liquid water (SLW) droplet conditions. The first generation of major aerospace icing models were developed by NASA Lewis Research Centre, the Office National d'Etudes et de Recherches Aérospatiales (ONERA) and the Royal Aircraft Establishment (RAE) [16]. All share common building blocks, comprising (a) a flowfield solution, (b) particle tracking (either in a Lagrangian or Eulerian framework), (c) a thermodynamic ice accretion model and (d) prediction of the ice profile and growth rate. This is shown in Fig. 1. In the SLW problem, high-altitude supercooled water droplets freeze on impact with cold aircraft surfaces. Whilst this is materially different from the problem of ice crystal accretion inside turbofan engines, the underlying building blocks may remain the same.

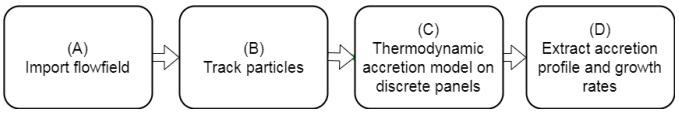

Fig. 1 Common building blocks of major aerospace icing codes

Fig. 2 shows the overall structure of ICICLE, using a similar four-column representation as Fig. 1, with blocks grouped by the type of physics – e.g. particle-air interactions. Both Fig. 1 and Fig. 2 are termed 'one-way coupled' models: mass, momentum, and energy of the particles (discrete phase) are altered by the flowfield; but the flowfield is not altered by the presence of particles or accretions. The accretion profile is generated by extrapolating the predicted growth rate over a fixed time period – the time for which the test article is 'exposed' to the icing cloud. It has been shown that this method can lead to inaccuracies for cases of 'large' accretions (of the same order of magnitude as the test article characteristic dimension) because (i) the area exposed to particles changes over time; and (ii) the assumption that the flowfield remains unchanged is unrealistic. Additionally, the effect of particle sublimation and evaporation on the flowfield temperature and humidity (i.e. energy and mass coupling respectively) is neglected.

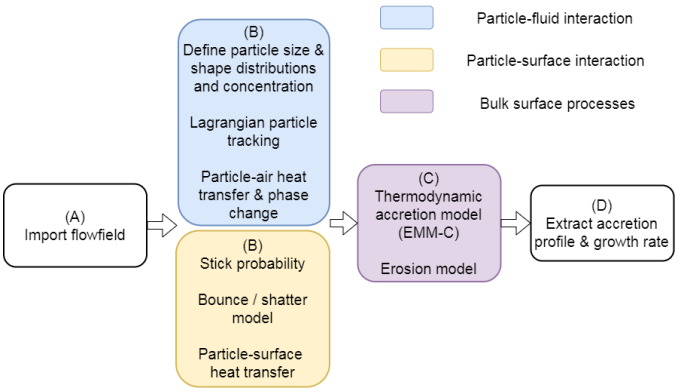

Fig. 2 Block diagram of the model. The blocks outlined in blue constitute the main timestepping loop.

Fig. 3 shows a higher fidelity method of two-way coupling. The new geometry (test article plus accretion) is re-meshed and the flowfield re-solved. Surface smoothing is typically required to aid mesh creation, and any gain in prediction accuracy is offset against an increased computational cost. The efficacy of this method is discussed in full in a companion paper [17]. An iterative two-way coupling of energy and mass is also implemented. Practically, this means that the flowfield temperature decreases and relative humidity increases if particles sublimate or evaporate.

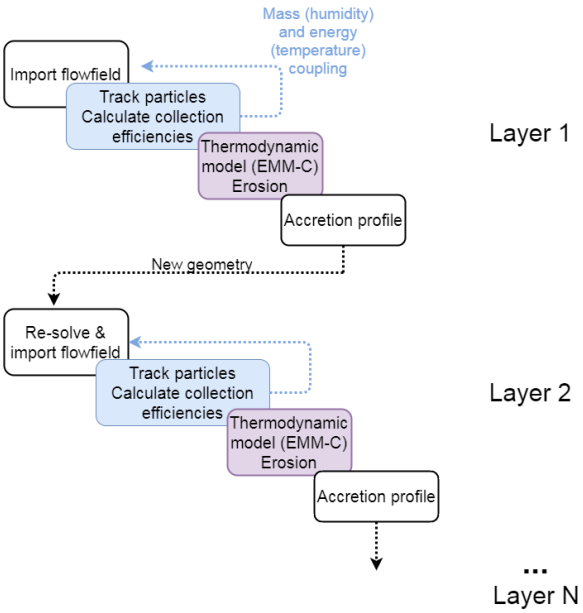

Fig. 3 Multi-layer accretion process using flowfield updating, and iterative two-way coupling of mass and energy

Particle-Air Interaction

Particle Size Distributions

Ice particles, both in the atmosphere and icing wind tunnels, can vary in diameter by two to three orders of magnitude, from microns to millimetres. For non-spherical particles, the size is described by the equivalent diameter, D_{eq}, which is the diameter of a sphere with the same volume as the particle. It is therefore desirable to statistically represent the particle cloud with a size distribution, which may then be

sampled to obtain an individual particle's equivalent diameter. The median mass diameter statistic in the distribution is then referenced to equivalent diameters, i.e. MMD is represented by MMD_{eq}.

Accurate representation of the particle size distribution is important for multiple elements of the model. Particle trajectory and impact location, melt percentage, probability of sticking, bouncing or shattering and capacity to erode accretions are immediate examples. The most common type of distribution used is the Weibull distribution, termed the Rosin-Rammler distribution when applied to particulates [18]. It is regularly used to describe distributions generated by liquid sprays and comminution processes (grinding, crushing or cutting). The mass fraction of particles with diameter greater than d is given by

$$Y_d = e^{-(d/\bar{D})^n} \quad (1)$$

where $\bar{D}$ is the diameter constant, defined as the value of d at which $Y_d = e^{-1}$, and n is the spread parameter, given by

$$n = \frac{\ln(-ln(Y_d))}{\ln(d/\bar{D})} \quad (2)$$

Size data for atmospheric particles are taken from flight tests 'flight 13' and 'flight 16', conducted by the High Altitude Ice Crystals (HAIC) and High Ice Water Content (HIWC) consortia in 2014 [19]. Here, the uncertainty in the measured equivalent diameter of each particle is reported as 5%. Fig. 4 shows the measured size distributions for flights 13 and 16, overlaid with their respective approximated Rosin-Rammler distributions. Particle diameter, D_{eq}, is plotted against the mass fraction of particles with a diameter greater than D_{eq}. The parameters of the fitted distributions and the mean error for each flight are given in Table 1. It may be seen that the Rosin-Rammler distribution is capable of closely representing two quite dissimilar distributions. Further flight test data in both similar and dissimilar convective systems are still required to assess if this is robustly applicable.

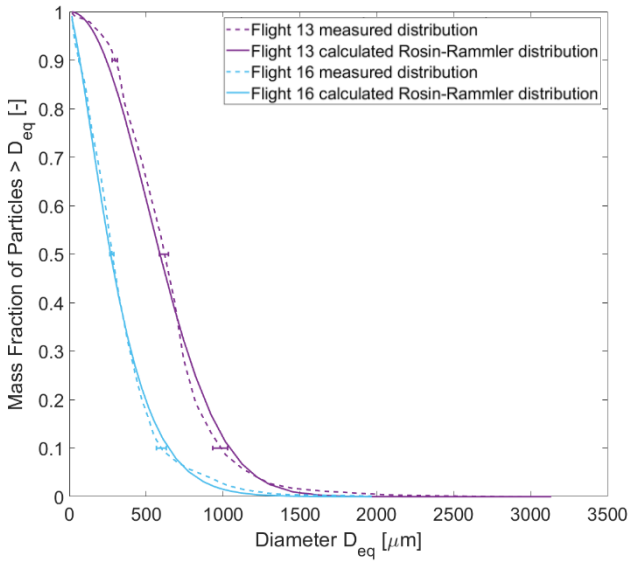

Fig. 4 Measured atmospheric PSDs in HAIC/HIWC flights 13 and 16 [19] and fitted Rosin-Rammler distributions.

Table 1 Parameters for Rosin-Rammler fits to HIWC/HAIC flight tests [19]

Case	D_{min} [μm]	D_{max} [μm]	$\bar{D}$ [μm]	n	N_{bins}	Mean error [%]
Flight 13	14	3100	700	2.1	42	1.4
Flight 16	14	1950	350	1.4	42	1.3

It is also instructive to consider how the particle size distribution (PSD) may change between the engine inlet and inlet to the intermediate or high pressure compressor. This provides a boundary condition for simulations considering only the core compression system. Aouizerate et al [20] used a Rosin-Rammler distribution with $MMD_{eq} = 400$ μm as the inlet icing cloud for a study of crystal ingestion, where a fan and single stage LP booster of a medium bypass ratio turbofan were modelled. A particle breakup model first proposed by Villedieu et al [5] was used to output the expected PSD at the fan face, downstream of the fan and downstream of the inlet guide vane (IGV). Fitting a Rosin-Rammler distribution to these distributions results in an error of less than 3%.

Particle Shape Characterisation

Atmospheric ice particles are inherently non-spherical. Shadowgraph images of particles captured during the HAIC/HIWC flight tests show a prevalence of columns, shards, and a smaller proportion of rounded or isometric shapes [19].

The influence of shape in the current work is principally limited to trajectory and heat transfer. However, it has other effects currently not accounted for: for example in-flight tumbling, and orientation-dependent impact behaviour. Similarly to [5], ice particles are approximated as spheroids in the current work. The attraction of this approach is that a single set of equations defines the particle shape and geometric parameters, and for a given equivalent diameter, D_{eq}, the shape is then defined solely by aspect ratio, E, as shown in Fig. 5. For

a value of E less than unity (oblate), discs or plates may be approximated; for values of E greater than unity (prolate), columns may be approximated.

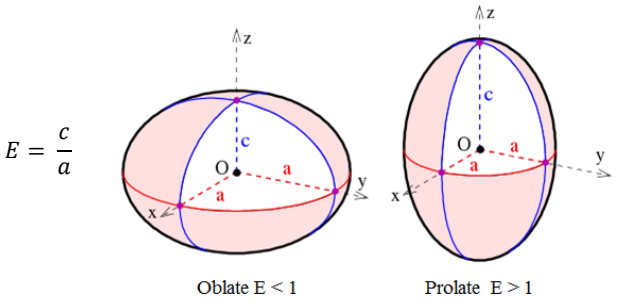

Fig. 5 Geometry of oblate and prolate spheroids of aspect ratio E

The particle volume is given by

$$V_p = V_{eq} = \frac{\pi}{6} {D_{eq}}^3 = \frac{4}{3}\pi a^2 c = \frac{4}{3}\pi a^3 E \tag{3}$$

where a and c are the equatorial radius and length from centre to pole respectively.

Particle shape is commonly described through reference to a sphere of the same volume. Two definitions, sphericity, φ [21] and crosswise sphericity, $\varphi_\perp$, [22] are used, where

$$\varphi = \frac{6\, V_{eq}}{D_{eq} A_p} \tag{4}$$

where A_p is the surface area and $V_{eq} = V_p = {}^1\!/_6\, \pi {D_{eq}}^3$. Substituting this in to equation (3),

$$\varphi = \frac{\pi {D_{eq}}^2}{A_p} \tag{5}$$

Sphericity is independent of particle orientation, and therefore cannot take into account differing drag coefficients should a particle (such as a plate or column) travel in a lengthwise (head on) orientation – where skin friction may dominate - rather than a crosswise (broadside) orientation – where form drag may dominate. Lengthwise plates, discs and some high-aspect ratio spheroids can attain a lower drag coefficient than a sphere (at the same particle Reynolds number), which also cannot be captured through sole use of sphericity [23]. Crosswise sphericity is defined as the ratio of the cross-sectional area of the volume-equivalent sphere and the actual area of the particle, projected normal to the flow direction ($A_{p,\perp}$):

$$\varphi_\perp = \frac{{}^\pi\!/_4\, {D_{eq}}^2}{A_{p,\perp}} \tag{6}$$

Since the particle orientation with respect to the flow is not known a-priori, an assumed orientation would need to be applied at the particle injection plane, and a tumbling model would then define the orientation at any timestep. Since a tumbling model is not included in the present work, it is assumed that particles adopt the (theoretically) most stable orientation, broadside to the flow. This is likely to be acceptable in steady flow cases, but in highly unsteady flows (such as the compressor environment) where perturbations knock particles from their stable orientations this may assumption may be limiting. Impacts with solid bodies (e.g. rotors) or regions of high flow curvature may also lead to particles being misaligned from the stable orientation. It is assumed that impacts that result in fragmentation produce secondary particles whose aspect ratio moves towards unity (for example, a columnar particle would be assumed to fragment into two shorter columns).

For spheroids, it may be shown that

$$\varphi_{oblate} = \frac{4E^{\frac{2}{3}}}{2 + {E^2}/{e} \ln\left(\frac{1+e}{1-e}\right)} \quad ; \quad \varphi_{\perp,oblate} = {E^{2}}/{3} \tag{7}$$

$$\varphi_{prolate} = \frac{2E^{2/3}}{1 + \mathrm{E}(\frac{\sin^{-1} e}{e})} \quad ; \quad \varphi_{\perp,prolate} = {E^{-1}}/{3} \tag{8}$$

where the eccentricity, e, is given by

$$e = \sqrt{1 - \min(E^2, {1}/{E^2})} \tag{9}$$

The crosswise sphericities are calculated assuming broadside travel. Given E and D_{eq}, equation (3) gives a; all other shape parameters may then follow. In ICICLE therefore, a distribution of D_{eq} and E need only be specified to characterize the seeded particles. At the particle injection plane, discrete injection points are defined; at each point, sufficient particles are released to represent the whole distribution.

Lagrangian Particle Tracking

In Lagrangian tracking, Newton's second law of motion is calculated for each particle at each timestep to determine its trajectory in the next timestep:

$$\sum \vec{F}_{x,i} = m_p \frac{d\vec{U}_x}{dt} \tag{10}$$

where $\vec{F}_{x,i}$ is the ith force term in the $\vec{x}$ direction, and $\vec{U}_x$ is the velocity in the same direction. The particle mass is given by $m_p = {}^1\!/_6\, \rho_p \pi {D_{eq}}^3$.

A spatially adaptive timestep is used to limit particle travel:

$$t_t = K_t \left({d_{min}}/{U_t}\right) \tag{11}$$

where U_t is the local velocity magnitude, d_{min} is the smallest grid cell dimension in the domain, and K_t is a user-defined constant – similar to a CFL number. The lower the value of K_t, the higher the trajectory accuracy (at a penalty of computational cost). The value of K_t required for an acceptable statistical convergence is dependent upon the time integration method, as discussed in the following section.

Time Integration of Particle Motion

The time integration strategy used in ice accretion codes is infrequently studied. A smaller time-step size can guarantee the stability and accuracy, but requires a larger number of tracking steps, increasing the computational time required. Given that the particle tracking stage of the code (i.e. prior to any thermodynamic accretion model) typically constitutes the majority of the overall runtime, significant gains may be obtained through proper selection of the time integration method. This is particularly true for cases where two-way coupling is

implemented during the particle tracking phase, necessitating iteration of the particle tracks.

Particle relaxation time - considering only drag- is given by

$$\tau_p = \frac{\rho_p {D_{eq}}^2}{18\mu_f} \tag{11}$$

in Stokes flow ($Re_p \ll 1$) and by

$$\tau_p = \frac{4}{3}\frac{\rho_p {D_{eq}}^2}{Re_p C_d \mu_f} \tag{12}$$

for $Re_p > 1$.

Trontin et al. [24] suggest an analytic integration method due to its advantages in stability, compared to higher order explicit schemes. For developing ICICLE, a comparison of first order schemes (including implicit and explicit Euler method and analytic method), second order trapezoidal scheme and fourth order Runge-Kutta scheme have been carried out for modelling ice accretion. Equation 13 shows the integrated form of the particle momentum equation for (a) the explicit Euler method, (b) implicit Euler method, (c) the analytic discretization method and (d) the second order trapezoidal scheme, respectively.

$$V_p^{n+1} = V_p^n + a_p^n \cdot \Delta t \tag{13(a)}$$

$$V_p^{n+1} = (V_p^n + \Delta t \cdot (g + V_f/\tau_p))/(1 + \Delta t/\tau_p) \tag{13(b)}$$

$$V_p^{n+1} = V_f + \exp\left(-\frac{\Delta t}{\tau_p}\right) \cdot \left(V_p^n - V_f\right) + \left(1 - \exp\left(-\frac{\Delta t}{\tau_p}\right)\right) \cdot g \cdot \tau_p \tag{13(c)}$$

$$V_p^{n+1} = \frac{V_p^n \cdot \left(1 - \frac{\Delta t}{2\tau_p}\right) + \frac{\Delta t}{2\tau_p} \cdot \left(V_f + \frac{1}{2}\Delta t \cdot V_p^n \cdot \nabla V_f\right) + \Delta t \cdot g}{1 + \frac{\Delta t}{2\tau_p}} \tag{13(d)}$$

The stability and accuracy of the explicit method is constrained by time-step size, especially for small particles. Similarly, other methods are hampered by the $1/\tau_p$ term, which may cause stability problems for particles of small diameter (due to evaporation or sublimation). In this scenario, dynamically switching to an Euler or trapezoidal formulation may be beneficial.

Fig. 6 shows the mass change over time of an ice particle, initially 2 µm equivalent diameter, sublimating in a dry airflow. The aerodynamic conditions are a total temperature of 257 K, total pressure of 47 kPa and freestream Mach number of 0.2. The phase change model is discussed in an ensuing section. For each time integration, solutions using differing values of the timestep multiplier, K_t, are plotted. It may be observed that implicit Euler, analytical and trapezoidal methods achieve similar convergence and permit values of K_t up to ~ 10, reducing the number of required steps by the same factor and thus reducing runtime. The explicit Euler method requires K_t to not exceed unity.

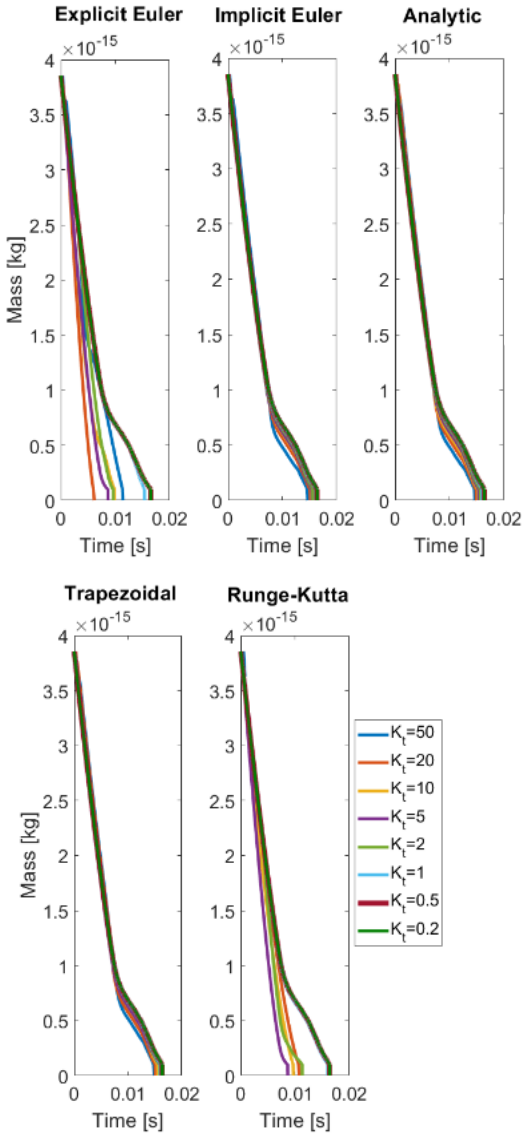

Fig. 6 Comparison of time taken to sublimate an ice particle at varying values of timestep multiplier (K_t)

Particle Forces

Equation (10) requires an assessment of the body forces pertinent to ice crystal motion. It is instructive at this point to consider whether particle motion is ballistic (inertia-dominated), or streamline-following (viscously dominated). This is typically quantified by the Stokes number, defined as

$$\mathrm{Stk} = \frac{\tau_p}{\tau_f} \tag{14}$$

where τ_p is as defined in equation (11) and the fluid characteristic time is given by

$$\tau_f = \frac{L}{\overline{U_f}} \tag{15}$$

where L is a characteristic length in the flowfield and $\overline{U}_f$ is a bulk flowfield velocity. An ice particle trajectory in a typical turbofan compressor may be used to get an expected approximate range. In this case, the characteristic flow dimension is taken as the axial chord of a typical intermediate pressure compressor stator vane, such that $L = C_x = 40$ mm. It is assumed that D_p is in the range $10 - 100$ μm, $\rho_p = 920$ kg/m^3, $\mu_f(T) = \mu_f(260\text{ K}) = 1.65x10^{-5}$ kg/m.s and $\vec{U}_f = 150$ m/s. Substituting these values into equations (11) and (14) yields Stokes number in the range $1.05 - 105$. This demonstrates that all but the smallest particles ($D_p < 10$ μm) will have near ballistic trajectories.

Drag and gravity will be considered as particle body forces. The high Stokes number range in the above analysis implies that accretion will be inertia driven. In this case, thermophoresis, turbophoresis, the Basset history force and Saffman's lift force may safely be neglected. Since $\rho_p \gg \rho_{air}$, the virtual mass force and Brownian motion may also be neglected [25], [26].

Drag

The drag force in the $\vec{x}$ direction may be expressed as

$$\vec{F}_{d,x} = -\frac{1}{2}\rho_f C_D\, A_{p,\perp} \left|\vec{U}_{p,x} - \vec{U}_{f,x}\right|(\vec{U}_{p,x} - \vec{U}_{f,x}) \tag{16}$$

where $A_{p,\perp}$ is the particle area projected normal to the flow and C_D is the drag coefficient. Drag coefficient correlations for spherical particles are widely available, notably that of Clift and Gauvin [27]. As part of the HAIC project, an assessment of available correlations for drag coefficient was performed [5], [13]. The correlation of Hölzer and Sommerfeld [23] is currently accepted as having the highest accuracy at the widest range of particle shapes. The correlation takes crosswise sphericity into account, to take into account the differing drag mechanisms (form drag or skin friction) depending on the orientation. It is given by

$$C_D = \frac{8}{Re_p}\frac{1}{\sqrt{\varphi_\perp}} + \frac{16}{Re_p}\frac{1}{\sqrt{\varphi}} + \frac{3}{\sqrt{Re_p}}\frac{1}{\varphi^{0.75}} + 0.42\left(10^{0.4(-log_{10}(\varphi))^{0.2}}\right)\frac{1}{\varphi_\perp} \tag{17}$$

where the particle Reynolds number, $Re_p = {\rho_f\left|\vec{U}_p - \vec{U}_f\right|D_{eq}}/{\mu_f}$.

The correlation is applicable up to the critical particle Reynolds number (~100 - 300 for the particle shapes considered here [28] and the full range of particle sphericities. The mean error of this correlation from 2061 experimental datapoints, covering spheres, spheroids, isometric particles, disks and plates, is given as 14.4 %. Previous correlations ([29], [30]) could incur errors of over 1000% for disks and plates.

Particle Phase Change Model

The following phase change model uses the method of Villedieu et al [5], which is itself an extension of Mason's hailstone melting model [14]. It will briefly be described here. A notional ice particle of arbitrary shape is approximated as a spheroid of the same volume, equivalent diameter, D_{eq}, and initial aspect ratio E_0. The particle has uniform internal temperature T_p. Initially fully glaciated, the particle temperature increases until it reaches the melting temperature T_f. During the fully glaciated stage (referred to as stage 1), the aspect ratio remains held at an initial value, E_0 but D_{eq} can change due to sublimation or deposition. During the melting stage (stage 2), a concentric water layer surrounds an ice core, with volumes $V_{p,i}$ and $V_{p,w}$ respectively. Eccentricity of the water layer or circulation within the layer is neglected [31]. The particle temperature is fixed at T_f in both the ice and water layers. The latent heat of fusion required for melting is balanced by evaporative and convective heat fluxes. During melting, the particle aspect ratio monotonically approaches unity, on the assumption that when the particle is fully melted it is a spherical droplet. Once fully melted (stage 3), the temperature is allowed to rise once again, and aspect ratio is held at unity.

In the stage 1, the continuity and energy equations are given respectively by

$$\frac{dm_p}{dt} = -\dot{m}_{sub} \;\; ; \;\; m_{p,i} = m_p \;\; ; \;\; m_{p,w} = 0 \tag{18}$$

$$m_p c_{p,i}\frac{dT_p}{dt} = Q_{conv} - \dot{m}_{sub}\, L_{sub} \tag{19}$$

and aspect ratio is held constant at $E = E_0$. The particle mass is given by $m_p = \rho_i \frac{\pi D_{eq}^3}{6}$, where ρ_i is the density of ice, taken as 920 kg/m^3. The sublimating or evaporating mass flux is given by

$$\begin{aligned}\dot{m}_{sub,evap} &= A_p H_m \rho_f(\omega_p - \omega_\infty) \\ &= L_v \frac{\pi D_{eq}^2}{\varphi}\overline{Sh}\,\frac{\rho_f D_{v,a}}{D_{eq}}(\omega_p - \omega_\infty) \\ &= L_v \frac{\pi D_{eq}}{\varphi}\overline{Sh}\,\rho_f D_{v,a}(\omega_p - \omega_\infty)\end{aligned} \tag{20}$$

where the average Sherwood number is given by [5]

$$\overline{Sh} = 2\sqrt{\varphi} + 0.55\, Sc^{1/3}\varphi^{1/4}\sqrt{Re_p} \tag{21}$$

and the local vapour mass fraction is given by

$$\omega = \frac{\dot{m}_{vap}}{\dot{m}_{dry,a}} = \frac{M_w}{M_a}\frac{P_{vap}}{P_{dry,a}} = \frac{M_w}{M_a}\frac{P_{vap}}{P - P_{vap}} \tag{22}$$

where M_w and M_a are the molar masses of water and dry air respectively and P is the local static pressure. P_{vap} is the partial pressure of vapour, given by

$$P_{vap} = RH\, P_{vap,sat} \tag{23}$$

where RH is the local relative humidity ($RH = 1$ at the particle surface and $RH \leq 1$ in the freestream), and $P_{vap,sat}$ is the local vapour pressure at saturation. This is calculated from the correlation given in Hyland and Wexler [32]. The local vapour diffusivity, $D_{v,a}$ is given as a function of local static temperature and pressure in [33].

The convective heat flux is given by

$$Q_{conv} = A_p\,\overline{H}\,(T_f - T_p) = \frac{\pi D_{eq}}{\varphi}\,\overline{Nu}\,k_f(T_f - T_p) \tag{24}$$

where the average Nusselt number is given by [5]

$$\overline{Nu} = 2\sqrt{\varphi} + 0.55\, Pr^{1/3}\varphi^{1/4}\sqrt{Re_p} \quad (25)$$

and the flow temperature local to the particle is taken as

$$T_f = T_s\left(1 + r_f\frac{\gamma_f - 1}{2}M_{rel}{}^2\right) \quad (26)$$

where the recovery factor, $r_f \cong Pr^{1/3}$ [34], T_s is the local static temperature and M_{rel} is the particle Mach number based on slip velocity. This equation yields $T_f = T_s$ when $M_{rel} = 0$ (i.e. no slip) and $T_f = T_r$ when $M_{rel} = M_\infty$ (stationary particles), where T_r is the recovery temperature.

In the second stage, the particle is in the process of melting and $T_p = T_f$. The continuity and energy equations are given respectively by

$$Q_{conv} = \dot{m}_{evap}L_v + \dot{m}_{melt}L_f \quad (27)$$

$$\frac{dm_p}{dt} = -\dot{m}_{evap}\ ; \frac{dm_{p,i}}{dt} = -\dot{m}_{melt}\ ;\ m_{p,w} = m_p - m_{p,i} \quad (28)$$

The particle melt ratio is given by

$$MR = \frac{m_{p,w}}{m_p} \quad (29)$$

In the third stage, the continuity and energy equations are given respectively by

$$m_p c_{p,w}\frac{dT_p}{dt} = Q_{conv} - \dot{m}_{evap}L_v \quad (30)$$

$$\frac{dm_p}{dt} = -\dot{m}_{evap}\quad ;\quad m_{p,w} = m_p\quad ;\quad m_{p,i} = 0 \quad (31)$$

and aspect ratio is held constant at $E = 1$. The particle mass is given by $m_p = \rho_w\frac{\pi D_{eq}{}^3}{6}$.

Quasi Two-Way Coupling of Mass & Energy

Thus far, a one-way coupled approach has only been considered. This means that the continuous (fluid) phase may change properties of the discrete (particle) phase, but not vice versa. A general assessment of coupling in a simple axial compressor in ice crystal icing conditions is given in Wright et al., (2010). Mass and momentum coupling are neglected on the basis that the mass loading fraction, $Z = {TWC}/{\rho_a} \ll 1$.

Energy coupling requires more careful consideration. It may be neglected if the following inequality is satisfied [35]:

$$\frac{Z}{St_m}\frac{L_{sub}}{C_{p,i}T} \ll 1 \quad (32)$$

where the mass transfer Stokes number is given by

$$St_m = \frac{\tau_m U_p}{L} \quad (33)$$

where U_p is an average particle velocity, L is a residence length (i.e. tunnel length or compressor length), and the mass transfer relaxation time is given by

$$\tau_m = \frac{\rho_i D_{eq}{}^2}{6\,Sh\,\rho_a D_{v,a}(\omega_p - \omega_\infty)} \quad (34)$$

In Wright et al [3], equation (32) is evaluated for a multistage compressor as ~0.1, implying that energy coupling is unimportant. However, in-service data from engines that have encountered ice crystal conditions show that the compressor delivery temperature can reduce during an ice crystal encounter (and may suffer a spike reduction if there is an ice shed). Use of this temperature reading as an ice crystal detection parameter has been proposed by Califf and Knezevici [36]. It is therefore apparent that in the 'real' engine environment, energy coupling cannot be neglected.

In AGARD advisory report AR-332 it is stated that an increase in humidity can also appreciably affect engine performance due to changing fluid properties [37]. It is stated that the parameters with the largest effects are the increasing gas constant, R_f, and the isentropic exponent, γ_f. The latter decreases from its dry air value of 1.4 towards the gaseous water value of 1.333. Both these changes cause the specific heat at constant pressure, C_p, to increase. It is therefore preferable to use enthalpy, rather than temperature, when solving energy coupling.

Two-Way Coupling: Energy

A simple approach is used to calculate the transfer of enthalpy from the airflow to particles, similar to that used to characterize icing wind tunnels [38].

The heat flux transferred from air to particles in the coupled case is given by

$$\begin{aligned} Q_{air} &= \dot{m}_a\left(h_{f,exit} - h_{f,exit,dry}\right) = -Q_p \\ &= -\frac{1}{\Delta t_{exp}}\sum_{p=1}^{p=N_p} SF_p\left[m_{p,i}C_{p,i}\left(T_{i,exit} - T_{i,inlet}\right)\right. \\ &+ L_f m_{p,w} + m_{p,w}C_{p,w}\left(T_{w,exit} - T_f\right) \\ &+ \left. L_{v,s}\left(m_{p,exit} - m_{p,inlet}\right)\right] \end{aligned} \quad (35)$$

where $\dot{m}_a$ is the mass flow rate of air, $h_{f,exit}$ is the enthalpy at the domain exit, $m_{p,w}$ is the proportion of the particle mass that is water, N_p is the total number of numerical particles and Δt_{exp} is the exposure time to the ice cloud. A 'packet mass' or 'parcel mass' approach is used to relate the mass of the numerical particles injected to the 'real' mass of particles injected in the simulated icing exposure. This is quantified through the scale factor, SF_p, given by

$$SF_p = \frac{m_{inj,parcel}}{m_{inj,p}} \quad (36)$$

where $m_{inj,parcel}$ is the fraction of the total 'real' mass with the same diameter as the particle in question.

Equation (35) reads that the heat extracted from the air is equal to the sum of the heat transferred to each particle per unit time. This in turn comprises (i) sensible warming of the ice particle at inlet temperature $T_{i,inlet}$ to outlet temperature $T_{i,exit}$ (note $T_{i,exit} = T_f$ if melting has begun), (ii) the latent heat of fusion required to melt a mass $m_{p,w}$, (iii) sensible warming of water to its outlet temperature $T_{w,exit}$ and (iv) particle evaporation or sublimation between inlet and exit. Note $L_{v,s} =$

L_s until the particle starts to melt; thereafter $L_{v,s} = L_v$. A summation is used since all the information required has already been calculated on a particle-by-particle basis in the phase change model.

Two-Way Coupling: Mass (Humidity)

Similarly to air temperature, the bulk specific humidity at exit may be calculated by summing the individual contributions from particle sublimation and evaporation. The change in vapour mass fraction is given by

$$\omega_{exit} - \omega_{exit,dry} = \omega_{exit} - \omega_{inlet} = -\frac{1}{\Delta t_{exp}} \frac{1}{\dot{m}_a} \sum_{p=1}^{p=N_p} SF_p (m_{p,exit} - m_{p,inlet}) \quad (37)$$

and the specific humidity at exit is given by

$$SH_{exit} = \frac{\omega_{exit}}{1 + \omega_{exit}} \quad (38)$$

Implementation

Since the system of equations are coupled, an iterative scheme is used. The particle trajectory and phase change calculations are performed for each iteration.

It is important to note that the flowfield is not re-calculated – so Mach number, pressure and density are unchanged despite the local change in temperature and gas properties. This is clearly acceptable provided changes are small. The effect of implementing this method in an icing wind tunnel is discussed in Appendix B. It is shown that the changes in both static temperature and specific humidity are not negligible – and thus the rather simplistic approach of equation (32) is not acceptable.

Particle-Surface Interaction

Particle-surface interaction is used as a catch-all term for the mechanical and thermodynamic processes that a particle undergoes when it impinges on a solid (undeflecting) surface. Processes are applied on a particle-by-particle basis and finish either when the particle has stuck to a surface or has been re-emitted into the airflow. The bulk process of ice accretion (i.e. how sticking particles become a homogenous ice layer), as well as erosion, are considered in later sections. This is illustrated in Fig. 7.

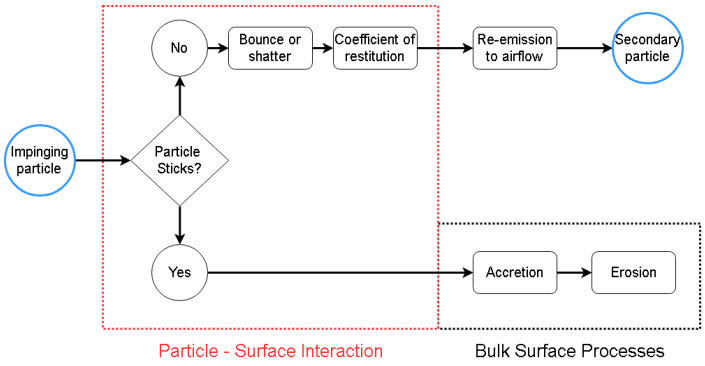

Fig. 7 Schematic of processes considered as particle-surface interaction

Note that only sticking or bouncing/shattering are considered. Other mass removal processes such as sliding, rolling, or submersion in runback water are not considered explicitly due to the modelling complexity and the difficulties in experimental validation. They are assumed to be included in the bounce and shatter mass flux.

Sticking

Sticking probability is a necessary precursor to a thermodynamic accretion model. Consider the case of ice particles impinging on a sub-freezing surface – the vast majority will bounce off.

When a particle impinges on a wall, a sticking probability, P_s, is calculated. The value of P_s is used to calculate the portion of the parcel mass that sticks to the wall, and the proportion that is re-emitted to the airflow. This is achieved through modifying the scale factor. The scale factor of the re-emitted particle is given by

$$SF_p' = SF_p(1 - P_s) \quad (43)$$

An alternative method is to compare P_s to a randomly generated number to decide if the particle sticks or bounces. This stochastic method may be discarded in favour of equation (43) as nearly double the number of particles are required to achieve statistical convergence.

Two distinct cases must be considered for particle sticking – a surface temperature above freezing ('warm'), and a surface temperature below freezing ('cold'). The former is more akin to the believed mechanism of engine ice crystal icing, whereby partially-melted ice particles are incident on initially warm surfaces. The latter is more akin to supercooled liquid water (SLW) icing – where ice forms due to liquid incident on cold surfaces.

1. Sticking on surfaces below T_f

A simple model is used here. An assumption is made that solid ice particles bounce off cold surfaces, and that liquid water fully sticks. The sticking mass is then equal to the impinging liquid mass. The liquid mass is either a fully melted droplet or the meltwater on a particle, shed onto the surface.

$$m_{stuck} = m_{stuck,w} = P_{S,cold,L}\, MR\, m_p \quad (44)$$

where the sticking probability of liquid on cold surfaces, $P_{S,cold,L} = 1$, and MR is the particle melt ratio at impact.

2. Sticking on surfaces above T_f

It has been shown that air temperatures above freezing can be conducive to ice crystal accretion. This has been observed both in tunnel tests [9], [10] and in engine data analysis [1], [39]. However, models and data for particle sticking in these warm conditions – whether empirical or analytical – are generally scarce. An experimental campaign was conducted in 2017 to generate semi-empirical models for ice crystal sticking and erosion when impinging on initially warm surfaces, at engine-realistic conditions. The findings of the study are detailed in full in [40]. It was determined that the sticking probability could be expressed as a function of melt ratio, as given by

$$P_s = 183\,MR^5 - 494\,MR^4 + 478\,MR^3 - 196\,MR^2 + 30.2\,MR - 0.526 \quad \text{for } 0.02 \leq MR \leq 0.37 \qquad (45)$$

$$P_s = 0 \quad \text{for } 0 \leq MR < 0.02 \text{ and } 0.37 < MR \leq 1.00$$

Bounce & Shatter

A new bounce-shatter model applicable to ice crystal icing was developed as part of the work performed by the HAIC consortium [5], [41]. The model uses a non-dimensional parameter defined as the ratio of normal kinetic energy to surface energy. This parameter has been observed experimentally to define the change of regime from bounce to shatter for both ice particles [42] and hail [43]. It is given as

$$\mathcal{L} = \frac{\rho_p \pi \frac{1}{6} {D_{eq}}^3 \frac{1}{2} {U_{p,n}}^2}{\pi e_\sigma {D_{eq}}^2} = \frac{1}{12}\frac{\rho_p D_{eq} {U_{p,n}}^2}{e_\sigma} \qquad (46)$$

where $U_{p,n}$ is the particle velocity normal to the wall and e_σ is the surface energy per unit area, given in [5]. The ratio may be seen as equivalent to a Weber number for solid particles. At some critical value of this parameter, the energy released by crack propagation exceeds the total surface energy of the particle. The particle is treated as a solid sphere and therefore equation (46) is likely to overpredict the shattering threshold – for example shards or porous particles will shatter more readily – and does not capture the effect of particle orientation at the point of impact.

Three distinct regimes are defined: (i) a quasi-elastic bounce, (ii) a non-elastic bounce with internal fracturing and (iii) fragmentation. The boundary between (i) and (ii) is given as $\mathcal{L}_1 \cong 0.5$ and between cases (ii) and (iii) as $\mathcal{L}_2 \cong 90$.

Bouncing Regime

In the bouncing regime, the particle ice density and aspect ratio are left unchanged pre- and post-impact. In ICICLE, meltwater is assumed to shed onto the surface. The new particle mass and diameter are given by

$$m_p' = m_{p,i} \quad ; \quad D_{eq}' = D_{eq,i} \qquad (47)$$

where dash superscripts denote post-impact properties. The particle velocity normal and tangential to the surface are given by

$$U_{p,t}' = \epsilon_t U_{p,t} \quad ; \quad U_{p,n}' = -\epsilon_n U_{p,n} \qquad (48)$$

where the tangential and normal coefficients of restitution, ϵ_t and ϵ_n, are given as

$$\epsilon_t = 1 \qquad (49)$$

$$\epsilon_n = 1 \text{ for } \mathcal{L} < \mathcal{L}_1 \quad ; \quad \epsilon_n = \left(\frac{\mathcal{L}_1}{\mathcal{L}}\right)^{1/3} \text{ for } \mathcal{L}_1 < \mathcal{L} \qquad (50)$$

Shattering Regime

In the shattering regime, there is significant absorption of normal kinetic energy due to fragmentation. This results in shallow exit angles regardless of the inlet angle [44]. For impacts where $\mathcal{L} \gg \mathcal{L}_2$, as may be expected on airframes or engines, fragments may number in the hundreds [42], [44], which may be prohibitive for characterising the fragment size distribution. As a result, literature models or data for secondary particle diameter is limited. From a modelling perspective, computational cost may also be prohibitive if hundreds of new particles are created per impact.

In [5], the maximum diameter of any particle in the post-impact fragment cloud is given by

$$D_{eq,max}' = D_{eq}\left(\frac{\mathcal{L}_2}{\mathcal{L}}\right)^{2/11} \qquad (51)$$

In ICICLE, it is assumed that a single numerical particle is released, that is representative of the fragment cloud. It is assumed to have a diameter of half $D_{eq,max}$, and has a scale factor, SF_p, that accounts for the entire mass of the post-fragment cloud. Due to the complexity of predicting the shape of secondary particles, the released particle is assumed to maintain the same aspect ratio as the pre-impact particle.

It has been shown experimentally that the energy released on shattering may lead to the average tangential velocity of the fragment cloud exceeding the pre—impact tangential velocity [44]. In [5], the change is accounted for using an additional coefficient of restitution, ϵ_{nt}. Since the energy release is related to the severity of fragmentation, it can be related to $\mathcal{L}$. The overall tangential velocity post-impact is given by

$$U_{p,t}' = \epsilon_{tt} U_{p,t} + \epsilon_{nt} U_{p,n} \qquad (52)$$

where $\epsilon_{tt} = 1$ and

$$\epsilon_{nt} = 0.4\left(1 - \sqrt{\frac{\mathcal{L}_2}{\mathcal{L}}}\right) \qquad (53)$$

The normal coefficient of restitution is given by equation (50).

At this point it is instructive to consider which regimes are pertinent to engine ice crystal icing. Fig. 8 plots lines of $\mathcal{L} = \mathcal{L}_1$ and $\mathcal{L} = \mathcal{L}_2$ for equivalent diameter against normal velocity. It may be expected that the particle equivalent diameter at the inlet to an intermediate pressure compressor or low pressure booster is of the order of 10s of microns. Given that velocity magnitudes in the early core compressor may typically be in the range 80 – 160 m/s at a top of descent condition, high-slip impacts with static surfaces ($Stk \gg 1$) or impacts with rotors are likely to result in $\mathcal{L} > \mathcal{L}_2$, i.e. particle fragmentation. Impacts with low slip (i.e. $Stk \sim 1$) are more likely to cause inelastic rebound, $\mathcal{L}_1 < \mathcal{L} < \mathcal{L}_2$.

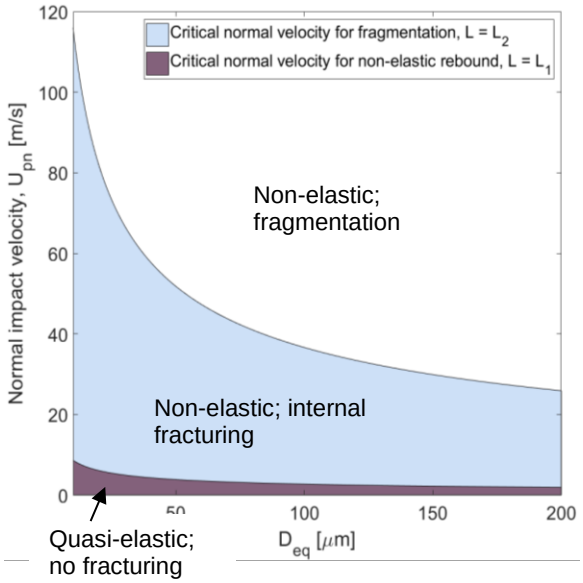

Fig. 8 Normal impact velocity against equivalent diameter for lines of $\mathcal{L} = \mathcal{L}_1$ and $\mathcal{L} = \mathcal{L}_2$ (after [5])

Extended Messinger Model for Ice Crystal Icing

Once the mass flux of ice and water sticking to a given location is known, a thermodynamic accretion model may be used to predict the bulk growth of ice and water layers. Existing models for ice crystal icing [3], [5] have typically used the Messinger Model (MM) [7], adapted to glaciated and mixed phase conditions. This is a steady approach where the substrate instantaneously adopts the equilibrium temperature of the accretion. This may be below the freezing temperature, T_f, for a rime ice accretion; equal to T_f for a glaze ice (ice layer plus surface water layer) accretion, and above T_f for running wet conditions.

For ICICLE, it was desired to improve on this in two ways:

1. Implement the Extended Messinger Model (EMM) of Myers [8], adapted to glaciated and mixed phase conditions. This is a quasi-steady model, which permits a linear temperature gradient through the accretion. The substrate temperature is therefore not confined to adopting the steady accretion temperature. For an initially warm engine surface, this allows a water film to first form whilst all particles are melted, followed by the initiation of an ice layer.
2. A necessary assumption of both the MM and EMM models is perfect thermal contact between the substrate and first accretion layer (whether ice or water). Previous implementations of the MM and EMM in mixed phase conditions have inherently assumed a substrate initially below freezing temperature, with ice as the first layer. This incorrectly models the physics of ice crystal icing on warm engine surfaces, where the first layer above the substrate must be water if the substrate is above freezing temperature.

A new thermodynamic model was created to adopt these two improvements, termed the Extended Messinger Model – Crystals (EMM-C). The EMM is adapted to glaciated and mixed phase conditions, and a novel three-layer (water-ice-water) system is proposed for substrates initially above freezing temperature, as shown in Fig. 9. Running wet conditions may also prevail in either scenario.

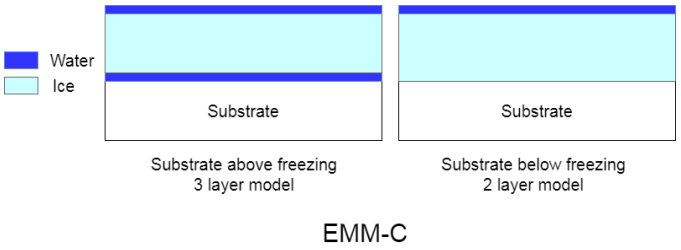

Fig. 9 Assumed accretion structure for substrates initially above or below freezing temperature

As with the classical EMM, the solution proceeds by solving a continuity equation, heat equations in each layer and a Stefan (phase change) equation. The model and its derivation are detailed in full in [45].

Erosion

It has been observed experimentally that erosion has a significant effect on the growth rate of accretions at engine-typical conditions [10], [40], [46]. Semi-empirical models have been proposed in [6], [10]. However, similarly to ice crystal sticking, there is a dearth of experimental data with which to build and tune models. De-coupling the driving parameters in sticking and erosion has also proved difficult in previous experimental campaigns [10].

Decoupling of sticking and erosion may be achieved – at least to a first approximation – by assuming that sticking probability is solely dependent upon bulk melt ratio (equation (45)). The primary mechanism of accretion mass loss is then assumed to be ductile erosion [10], dependent upon the velocity and diameter of the impinging particles, as well as the accretion temperature. A semi-empirical model was developed following testing of a conical test article in the NRC Research Altitude Test Facility, as detailed in [40]. Sticking and erosion are coupled to produce a 'net' sticking efficiency:

$$\eta_{s,net} = P_s(1 - \eta_{loss}) \tag{54}$$

where the mass loss efficiency, η_{loss}, is given by

$$\eta_{loss} = \min(1, \eta_{ero} + \mathcal{H}) \tag{55}$$

$$\eta_{ero} = A\left(1 + \log_{10}\left({KE}/{KE_0}\right)\right)(1 + B\sin^2\gamma)\left(e^{\left(-C\,{Q_S}/{R}\left({1}/{T_w} - {1}/{T_f}\right)\right)}\right) \tag{56}$$

where γ is the angle between the local surface normal and the axial directions, T_w is the accretion surface temperature, R is the specific gas constant of air and Q_S, the surface activation energy of ice, is 4.82E4 J/K.mol. KE is a quasi- kinetic energy parameter, defined as $KE = \overline{D_{eq}{}^3}U^2$, where $\overline{D_{eq}{}^3}$ is calculated by cubing the particle diameter for each bin in the distribution and mass averaging. Model constants KE_0, A, B and C may be found in [40].

Code Algorithm

Particles are seeded at the injection plane (usually coincidental with the inlet plane of the fluid domain). Lagrangian tracking, the phase change model, and two-way coupled mass/energy (if implemented) are performed on each particle until all particles have either stuck to a wall, left the domain or evaporated.

The thermodynamic accretion model, EMM-C, is then solved on discrete panels around the test article surface and/or domain walls (e.g. the hub and casing of an annulus). The mass of particles stuck to a given panel is scaled using SF to get the mass fluxes of ice and water under 'real' conditions, $\dot{m}_{i,panel}$ and $\dot{m}_{w,panel}$. EMM-C is solved per panel, using $\dot{m}_{i,panel}$, $\dot{m}_{w,panel}$, H_{panel}, $\omega_{e,panel}$, $T_{e,panel}$ and $P_{e,panel}$ as its primary inputs. H_{panel} is the average heat transfer coefficient at the panel location, and $\omega_{e,panel}$, $T_{e,panel}$ and $P_{e,panel}$ are the local freestream specific humidity, static temperature and static pressure respectively. The local heat transfer coefficient is provided by correlations in the case of simple geometries such as a wedge or cone; or by CFD for cases such as a blade or vane. At present, there is no correction of the predicted heat transfer coefficient distribution due to the roughness of accreted ice. Whilst roughness has been categorized for supercooled water accretions [15], [47], there is a lack of data for ice crystal accretions.

The model outputs the 'gross growth' (neglecting erosion) of ice and water. An erosive efficiency ($\eta_{ero,}$, between zero and unity) is then calculated individually for each point in the panel. Individual calculations are performed since points on curved panels will have a range of surface normals, and thus a range of erosive efficiencies. The 'net' ice and water layer growths for each point are then calculated, where it is assumed that erosion only changes the ice layer thickness.

Validation Test Case

ICICLE has been validated against ice crystal icing experiments conducted using a prismatic stator test article, installed in the Research Altitude Test Facility (RATFac) at the National Research Council of Canada (NRC) in Ottawa.

Fig. 10 shows the test article. The main body comprises a prismatic aerofoil, of 27.5° camber angle, chosen to be representative of a core compressor stator vane at midspan.

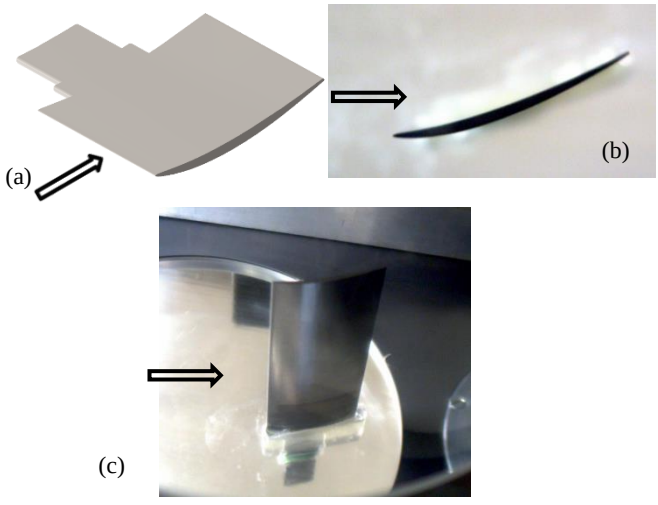

Fig. 10 (a) Isometric view of stator test article; (b) side (tip) view when installed in RATFac and (c) suction surface view. All arrows denote direction of flow.

A summary of the test conditions used for the test article is given in Table 2. Throughout the campaign, freestream total pressure was held at 34.5 kPa (ISA altitude of approximately 8.2 km / 27,000 ft) and total air temperature at 10 °C. For the results shown here, the Total Water Content (TWC) was maintained at 8 g/m^3 and the stator angle of attack at 0°. The stator was also tested at angles of attack between -20° and 20°. Full details of the test article, test conditions and results not reproduced here may be found in [48].

Table 2 Summary of test conditions for the stator test case

Parameter	*Minimum*	*Baseline*	*Maximum*
Freestream Mach [-]	0.25	0.40	0.40
Relative humidity [-]	0.05	0.22	0.65
Ice D_{v10} [µm]	18	18	35
Ice D_{v50} [µm]	34	34	68
Ice D_{v90} [µm]	54	54	131

ICICLE requires the flowfield around the stator and the heat transfer coefficient distribution at each aerodynamic condition as inputs. The computational setup and results are given in Appendix A.

Results

Particle Melt Ratio

To ensure an accurate accretion prediction, the rate of particle sticking- and hence melt ratio - at a given location must be well predicted. This in turn depends on the accuracy of the particle tracking and phase change models.

Approximate validation of predicted melt ratio is possible using the data recorded during the stator experiments. The word 'approximate' is used for two reasons. Firstly, the measured melt ratio is a single, bulk value. This can only be compared to a 'total' melt ratio in the simulation, calculated as the summed contributions of all numerical particles at the melt ratio measurement plane. Secondly, the Science Engineering Associates (SEA) multiwire probe used to measure the Liquid Water Content (LWC) suffers from a 'false response' – a liquid water reading when in fully glaciated conditions, as detailed in [10], [40], [49]. Since the probe cannot be calibrated against an independent device, the bias (systematic) uncertainty in LWC – and hence melt ratio- cannot be quantified.

Table 3 shows five test conditions of varying relative humidity, their respective measured and ICICLE-predicted melt ratios at the probe measurement plane. The measured values are corrected for the probe false response. All conditions other than humidity were maintained at their baseline conditions, as given in Table 2. A constant particle aspect ratio of 0.70 [50] was specified for the simulated particles, which were fully glaciated at the domain inlet.

Table 3 Measured and predicted melt ratio at LWC measurement plane for four test conditions

Case	*RH_0* [-]	*TWB_0* [°C]	*Melt ratio: experiment* [-]	*Melt ratio: ICICLE* [-]	*Difference (absolute)* [-]
1	0.05	-6.37	0.010	0.00	-0.010
2	0.15	-3.33	0.022	0.00	-0.022

3	0.45	2.64	0.10	0.070	-0.030
4	0.65	5.16	0.17	0.14	-0.030

For cases 1 and 2, there remains a small measured melt ratio at significantly negative total wet bulb temperatures (where melting is assumed to be inhibited). The measured values of 0.010 and 0.022 are within the scatter of the false response data [40], so are not further considered.

For cases 3 and 4, the model underpredicts the melt ratio at the probe plane by around 3% (absolute) - which is significant compared to the width of the plateau region of sticking efficiency (approximately 9-13% melt ratio). On the assumption that the aerodynamic conditions are well known and well controlled, then particle size and shape modelling is more likely to be the cause of the discrepancy. The size distribution below the 10th percentile is not known; if there is a significant negative skew in the actual PSD, (a higher concentration of smaller particles), then the measured melt ratio will be higher. Further, if the aspect ratio assumed in the model is too high, then the predicted melt ratio will be lowered. Modelling the particles as spheroids also introduces errors; especially if there is a predominance of slivers or shards (as may occur with a grinder ice system) with high surface area-to-volume ratios, or porous conglomerates of small particles. The calculated Nusselt and Sherwood numbers are also affected by shape; similarly the slip velocity is also dependent on shape (via drag coefficient). Additionally, the inhibition of in-flight tumbling may induce errors.

A study is currently being performed to model the effect of porosity on melt ratio. A porosity factor, PF, is defined as

$$PF = \frac{V_{p,i}}{V_p} \tag{57}$$

where $V_{p,i}$ is the volume of ice and V_p is the total volume – the sum of the particle volume and an air volume – where $V_p = V_{eq} = \frac{\pi}{6} {D_{eq}}^3$. If the particle is partially melted, the porosity factor only applies to the unmelted ice core. For a given equivalent diameter, therefore, increasing the value of PF results in a less dense, lighter particle. The density of the ice core is given by

$$\rho_{core} = (1 - PF)\rho_f + PF\rho_i \tag{58}$$

where ρ_f is the air density and ρ_i is the density of pure ice. The overall density of the particle is given by

$$\frac{1}{\rho_p} = \frac{(1 - MR)}{\rho_{core}} + \frac{MR}{\rho_w} \tag{59}$$

where MR is the melt ratio and ρ_w is the density of pure water.

The effect of porosity factor has thus far been investigated for the $RH_0 = 0.45$ condition. It was found that to match the experimentally measured melt ratio, the value of PF was 0.60. This appears quite low; however, as discussed above it is accounting for a number of disparate approximations. Furthermore, the exact shape characteristics of RATFac particles remains uncharacterized, and so the calculated value of PF may prove to be reasonable. Future work will involve calculating the required value of PF to match melt ratio at a wider range of test conditions. It is worth noting that a sensitivity analysis conducted on ICICLE concluded that the phase change model was most sensitive to humidity; however the error recorded in Table 3 is outside of the bias uncertainty of the humidity measurement and therefore cannot be wholly attributed to this.

Larger particles that are not incident on the test article and traverse the wake experience significant slip velocities. For example, a particle of 34 µm equivalent diameter that traverses the wake below the stator gains a peak slip velocity of 105 m/s, increased from a minimum of 2 m/s upstream of the stator. This results in a proportional rise in Reynolds number, Re_p, and corresponding increase in Nusselt (dependent on $\sqrt{Re_p}$). The air temperature also recovers towards total conditions. The resulting increase in convective heat transfer to the particles results in the rate of melting increasing by a factor of 1.8 in the wake compared to the freestream.

Growth Predictions on Baseline Case

Fig. 11 shows a test at the baseline aerodynamic and icing conditions at test end, viewed from (a) the top, onto the pressure surface; and (b) from the side, which is used for growth rate data extraction. It may be seen that the accretion at this condition is reasonably uniform from around 20% to 100% span (tip).

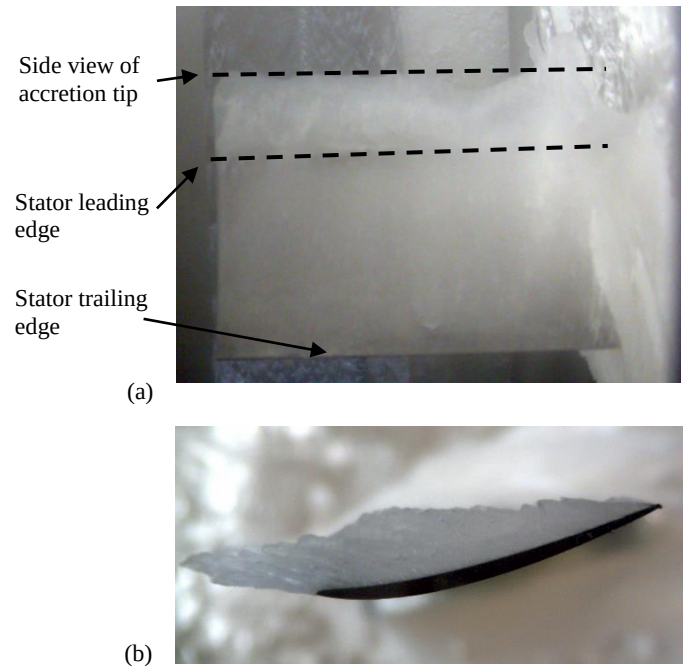

Fig. 11 Accretion for the baseline case at test end, viewed from (a) the top, onto the pressure surface, and (b) the side

Fig. 12 shows a comparison of ICICLE-predicted accretion profiles and experimental measurements at the baseline conditions. Comparisons are shown for discrete exposure times of 60 s, 120 s and 180 s. Axes are normalised by the stator axial chord. For each timepoint, the agreement is within 20% at any chordwise position.

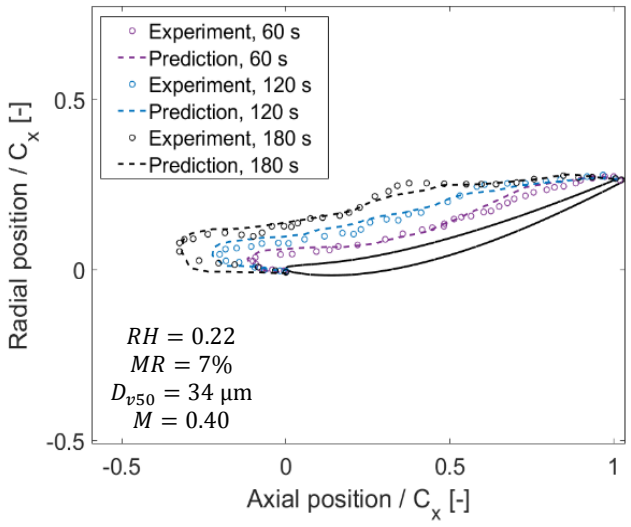

Fig. 12 Comparison of ICICLE-predicted and measured accretion profiles at discrete timesteps

Fig. 13 shows ICICLE-predicted and experimentally measured accretion growth histories for the same case. Data is shown at three chordwise positions, with errorbars plotted on every 20th datapoint of the 5% chord position. Gaps in the data – most notably in the 90% chord position – denote a failure of the postprocessing script to detect the edge of the ice accretion at that timestep. This is invariably due to obscuration of the camera window or a fluctuation in the icing cloud washing out the image background. At low accretion thicknesses the noise in the edge detection is also significant.

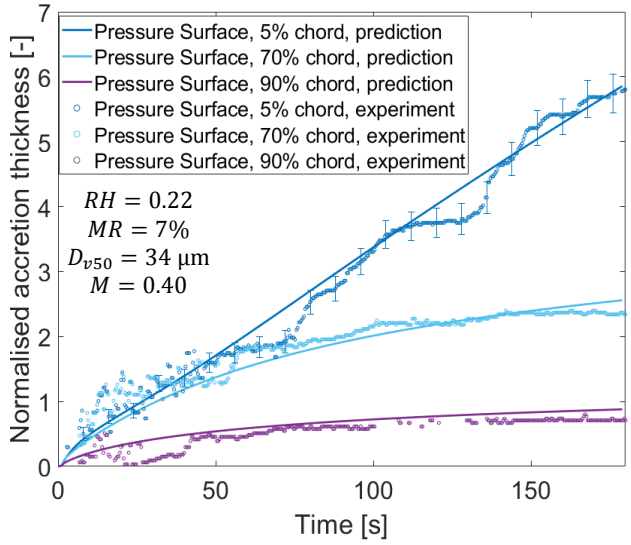

Fig. 13 Comparison of measured and predicted accretion thicknesses over the exposure time at three chordwise positions, for the baseline case

Varying Melt Ratio

Fig. 14 shows three comparisons of experimentally-measured and predicted accretion profiles for tests with measured particle melt ratios of (a) 0.01, (b) 0.04, and (c) 0.10. All other conditions were held at their baseline values to ensure no difference in the rate of erosion.

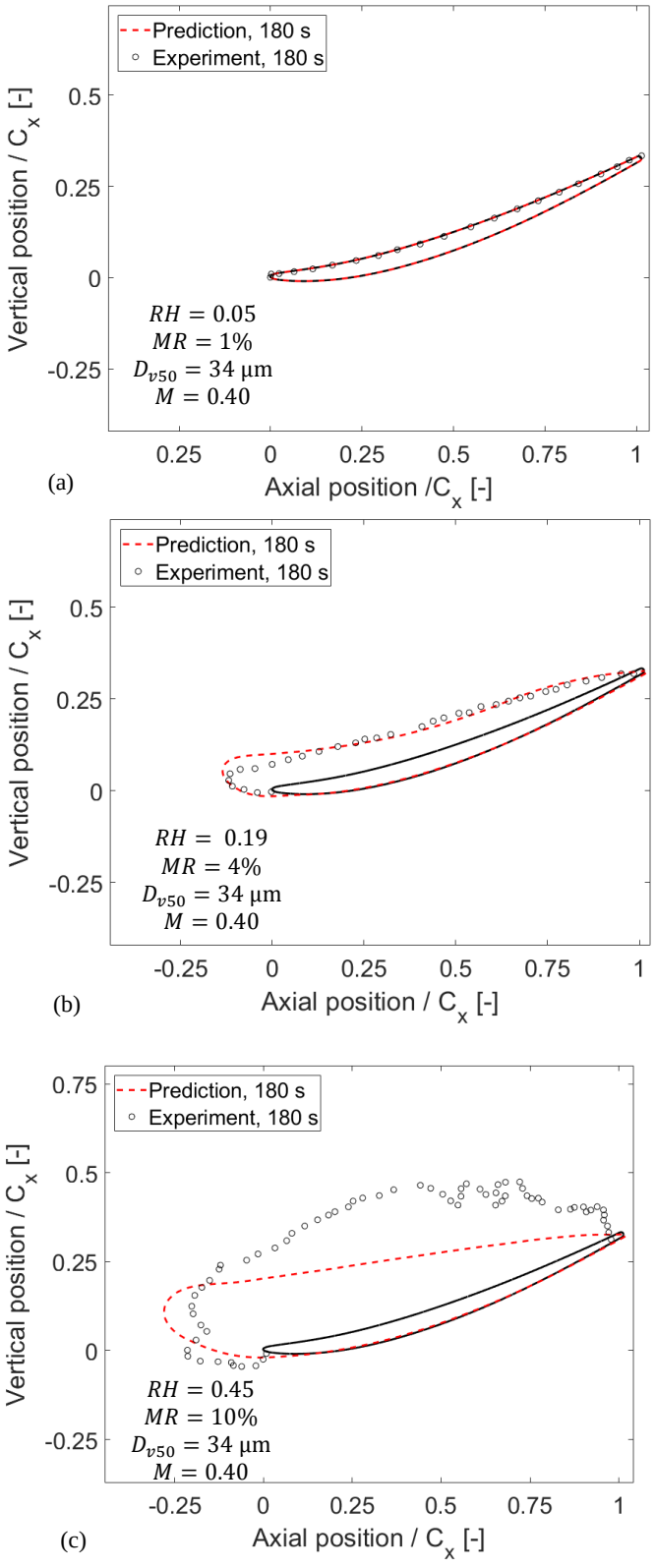

Fig. 14 Comparison of experimental and ICICLE-predicted accretion profiles on the stator test article after 180 s

In cases (a) and (b) the predictions give reasonable agreement with the experimental measurements, with a maximum error of ~ 30% at the leading edge of case (b). In case (c), the comparison between prediction and experiment is clearly poorer. This condition is in the plateau region of particle sticking, so a large accretion would be

expected. There is a shed at the leading edge during the test time so the agreement here would be expected to be poor. The case is also complicated by the fact that the accretion rotates forwards during the test, also increasing the collection efficiency on the top surface. The surface in contact with the aerofoil prior to rotation is shown by the black dashed line in Fig. 15.

On the pressure surface, the primary issue with the simulations is that growth that exceeds the projected area of the test article (for example growth vertically above the trailing edge) will occur very slowly. This is due to the profile edge being approximately aligned with the axial direction, maximising erosive efficiency and minimising collection efficiency. It is demonstrated in [17] that the agreement may be improved by re-calculating the flowfield and particle trajectories at discrete points during the test.

Fig. 15 Accretion at test end for the 10% melt ratio case. The original contact surface between accretion and aerofoil before rotation is shown by the black dashed line.

The new thermodynamic accretion model (EMM-C) also produces an estimate for the thickness of any internal water layer between the solid accretion and the test article. Table 4 shows the relative height of these water layers at the test end for three cases of varying relative humidity. The findings agree qualitatively with the observation that the 18% melt ratio case is more translucent (indicative of a water layer on the test article surface) and also slides and sheds more readily. The information in Table 4 could therefore potentially be used to develop or test future shedding models.

Table 4 Internal water layer height for three cases of varying relative humidity

Melt ratio	*Normalised internal water layer height,* h_{int} $[-]$
0.04	0.40
0.10	0.73
0.18	1

Conclusions

A new comprehensive numerical model for ice crystal icing has been developed. It incorporates Lagrangian tracking for non-spherical particles, phase change, and a stick, bounce and shatter model. Two-way coupling of mass and energy has been incorporated into an ice crystal icing model for the first time, modelling the effect on flow enthalpy and humidity as particles evaporate or sublimate. A new sticking model based on experimental data at engine-realistic conditions has been incorporated into the code, as well as a decoupled semi-empirical erosion model. A new thermodynamic model is also integrated, which uses a novel three-layer (water-ice-water) ice crystal accretion structure to account for ice growth on initially warm engine surfaces.

The particle tracking and phase change model has been validated against experimentally measured ice crystal melting in the NRC's Research Altitude Test Facility. A discrepancy of ~3% in melt ratio is observed, and a porosity model has been proposed as one possible correction for this.

The code as a whole has been validated against experiments conducted on a prismatic stator test article in the RATFac ice crystal wind tunnel. The performance of the code was studied for a test case at the baseline aerodynamic and icing conditions. For three chordwise locations on the stator pressure surface, experimental and predicted growth histories were compared, and found to agree within 20%. ICICLE was then applied to test cases with differing melt ratio. In the lower melt ratio cases the accretion profiles were well predicted, with the notable exception of a wet, slushier cases where the experimental accretion was invariably larger than the prediction.

The generally good agreement for an engine-realistic aerofoil is a significant advance for the ice crystal icing community, as previously codes have only been validated against more simple geometries (hemispheres, cones, cylinders). Previous attempts to predict ice growth in the engine environment have been restricted to qualitative assessments of likely impact locations, rather than a quantitative study of growth rates.

Contact Information

Corresponding author: Alexander Bucknell
Department of Engineering Science, Oxford Thermofluids Institute
alexander.bucknell@eng.ox.ac.uk

Acknowledgments

The authors would like to thank Rolls-Royce Plc for funding the research and the UK Engineering and Physical Sciences Research Council (EPSRC) for the Centre for Doctoral Training (CDT) in Gas Turbine Aerodynamics studentship (grant ref. EP/L015943/1).

Appendices

Appendix A – Computational Setup

The numerical domain is a thin (5mm) 3D slice of the stator test article installed in the Research Altitude Test Facility (RATFac). Using a 3D slice was found to aid convergence compared to a 2D case. Periodic boundary conditions were applied on the side walls of the domain. The entire length from cascade rig inlet to test article leading edge was modelled, necessitated by the requirement to match melt ratio, as well as the full cascade rig height.

A hybrid tetrahedral-prism unstructured mesh was used of 2.3M cells. 22 prism layers were applied at solid boundaries. The maximum y+ on the stator surface up to 90% chord was 1.5. Fig. A-1 shows the domain and Fig. A-2 the flowfield at the Mach 0.4 condition.

The solver was ANSYS Fluent v16.2, using density-based RANS. The k-ω SST turbulence model was used. Inlet boundary conditions were fixed at a total temperature of 283 K, total pressure of 34.5 kPa, and freestream Mach numbers of 0.25 & 0.40, matching the baseline aerodynamic conditions. The inlet turbulence intensity was set at 7.5%,

based on previous measurements in RATFac, with a lengthscale of 0.08 m [51] .

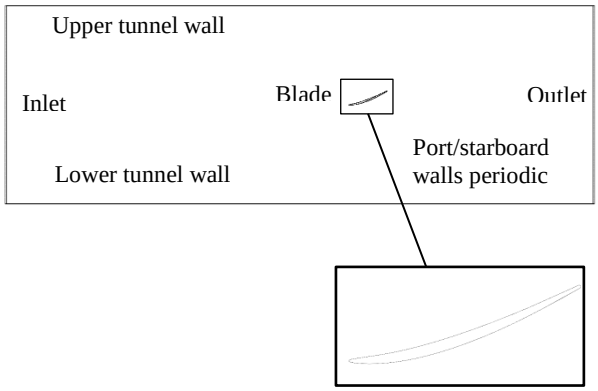

Fig. A-1 Numerical domain for stator, flow is left to right.

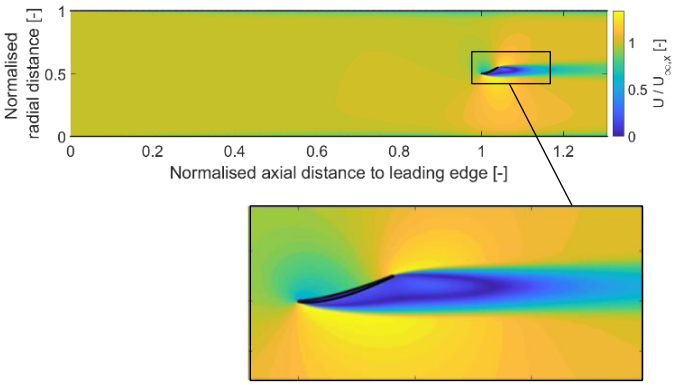

Fig. A-2 Contour of velocity normalised against axial velocity for the Mach 0.40 aerodynamic condition; flow is left to right.

The local heat transfer coefficient on the test article is also required as an input to ICICLE. It is used to calculate the convective, and evaporative heat fluxes on the icing surface. These terms are critical in determining whether ice will form, or whether complete melting (running wet conditions) will occur.

The heat transfer coefficient distribution was also extracted from the CFD simulations. A two-point approach was used: two simulations were run at the same aerodynamic condition, with differing isothermal wall temperatures (300 K and 310 K). The local heat transfer coefficient may be calculated using both conditions as given in equation (A1).

$$H(s) = \frac{q_{w,2}(s) - q_{w,1}(s)}{T_{w,2} - T_{w,1}} \quad \text{(A1)}$$

where s is the streamwise distance from the cone tip, $q_w(s)$ is the predicted heat flux and T_w is the uniform wall temperature. Heat flux was circumferentially averaged.

The values are held constant over the exposure time and so do not take into account changes in surface roughness, shape or the presence of a water film. A fully turbulent boundary layer was assumed since (i) the turbulence intensity in RATFac was measured to be approximately 7.5% at the tunnel centreline on the traverse plane [51], and (ii) the tunnel Reynolds number based on hydraulic diameter was varied in the range 4.0 x10^5 to 6.4 x10^5.

Fig A-3 shows the predicted heat transfer coefficient distribution for the Mach 0.40 simulation. For the pressure surface, a correlation for an inclined flat plate with favourable pressure gradient [52] is also plotted. The integrated difference is within 15%.

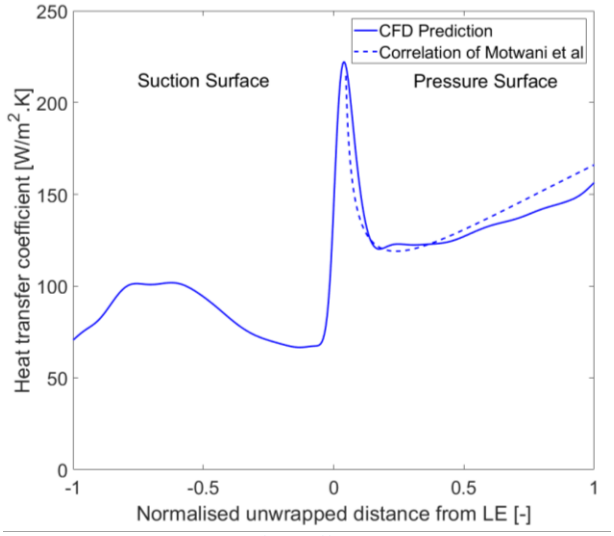

Fig A-3 CFD-predicted heat transfer coefficient distribution against streamwise location, with inclined flat plate correlation [52]

Appendix B: Effect of Two-Way Mass & Energy Coupling

At the baseline aerodynamic test conditions, a relative humidity of 45% and baseline particle size distribution, the effect of implementing two-way mass and energy coupling was investigated.

Fig B-1 shows the percentage change in specific heat capacity, specific humidity, static temperature and enthalpy at the exit plane of the domain. It may be seen that at this relatively high humidity, the effect of implementing two-way coupling is to allow condensation or deposition onto the particles, resulting in a decreasing specific humidity and decreasing flow enthalpy.

In absolute terms, there is a decrease in specific heat capacity of ~ 2.2 J/kg/K and a reduction in static temperature of ~ 1.8 K. Since the dry static temperature in this case is around 275 K, this shift is significant for the icing energy balance due to its proximity to freezing temperature. The analysis presented here demonstrates that the simplistic non-dimensional assessment of equation (32) is left wanting and may be an insufficient test to determine if energy coupling is required.

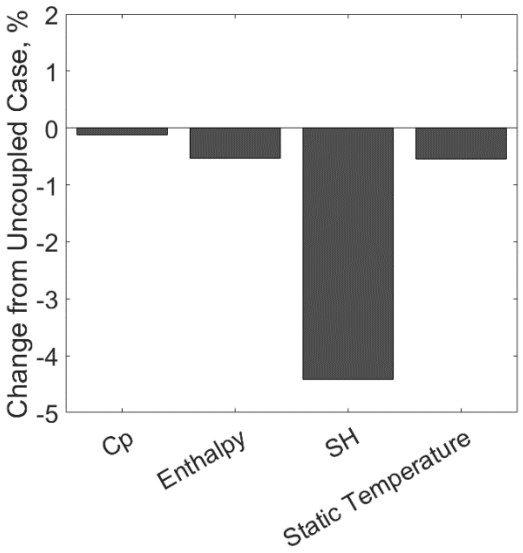

Fig. B-1 Percentage change in flow specific heat capacity, enthalpy, specific humidity (SH) and static temperature between coupled and uncoupled mass and energy cases.

References

[1] J. G. Mason, J. W. Strapp, and P. Chow, 'The Ice Particle Threat to Engines in Flight', presented at the 44th AIAA Aerospace Sciences Meeting and Exhibit, Reno, Nevada, 2006.

[2] R. S. Mazzawy, 'Modeling of Accretion and Shedding in Turbofan Engines with Mixed Phase/Glaciated (Ice Crystals) Conditions', presented at the SAE Aircraft and Engine International Icing Conference, Seville, Spain, 2007.

[3] W. B. Wright, P. C. E. Jorgenson, and J. P. Veres, 'Mixed Phase Modeling in GlennICE with Application to Engine Icing', presented at the AIAA Atmospheric and Space Environments Conference, Toronto, Ontario Canada, 2010.

[4] S. Nilamdeen and W. Habashi, 'Multiphase Approach Toward Simulating Ice Crystal Ingestion in Jet Engines', *AIAA Journal of Propulsion and Power*, vol. 27, no. 5, Sep. 2011.

[5] P. Villedieu, P. Trontin, and R. Chauvin, 'Glaciated and mixed-phase ice accretion modeling using ONERA 2D icing suite', presented at the 6th AIAA Atmospheric and Space Environments Conference, Atlanta, GA, 2014.

[6] P. Trontin, G. Blanchard, and P. Villedieu, 'A Comprehensive Numerical Model for Mixed Phase and Glaciated Icing Conditions', presented at the 8th AIAA Atmospheric and Space Environments Conference, Washington, D.C., USA, 2016.

[7] B. L. Messinger, 'Equilibrium Temperature of an Unheated Icing Surface as a Function of Air Speed', *J. Aeronaut. Sci*, vol. 120, no. 1, pp. 29–42, Jan. 1953.

[8] T. G. Myers, 'Extension to the Messinger Model for Aircraft Icing', *AIAA J.*, vol. 39, no. 2, pp. 211–218, Feb. 2001.

[9] P. M. Struk *et al.*, 'Fundamental Ice Crystal Accretion Physics Studies', presented at the SAE 2011 International Conference on Aircraft and Engine Icing and Ground Deicing, Chicago, IL, USA, 2011.

[10] T. Currie, D. Fuleki, and A. Mahallati, 'Experimental Studies of Mixed-Phase and Sticking Efficiency for Ice Crystal Accretion in Jet and Engines', presented at the 6th AIAA Atmospheric and Space Environments Conference, Atlanta, GA, 2014.

[11] K. Al-Khalil, E. Irani, and D. Miller, 'Mixed-Phase Icing Simulation and Testing at the Cox Icing Wind Tunnel', presented at the 41st AIAA Aerospace Sciences Meeting and Exhibit, Reno, Nevada, 2003.

[12] E. J. Grift, E. Norde, E. Van der Weide, and H. Hoeijmakers, 'Computational Method for Ice Crystal Trajectories in a Turbofan Compressor', no. SAE Technical Paper 2015-01-2139, 2015.

[13] E. Iuliano, E. Montreuil, E. Norde, E. Van der Weide, and H. Hoeijmakers, 'Modelling of Non-Spherical Particle Evolution for Ice Crystals Simulation with an Eulerian Approach', in *SAE Technical Paper 2015-01-2138*, 2015.

[14] B. J. Mason, 'On the Melting of Hailstones', *Quarterly Journal of the Royal Meterological Society*, vol. 82, pp. 209–216, 1956.

[15] R. W. Gent, N. P. Dart, and J. T. Cansdale, 'Aircraft icing', *Phil. Trans. R. Soc. Lond*, vol. 358, pp. 2873–2911, 2000.

[16] W. B. Wright, R. W. Gent, and D. Guffond, 'DRA/NASA/ONERA Collaboration on Icing Research. Part 2; Prediction of Airfoil Ice Accretion', NASA-CR-202349, May 1997.

[17] J. P. Connolly, A. Bucknell, M. McGilvray, D. R. H. Gillespie, B. Collier, and G. Jones, 'Two-way Flow Coupling in Ice Crystal Icing Simulation', presented at the International Conference on Icing of Aircraft, Engines, and Structures, Minneapolis, MN, 2019.

[18] P. Rosin and E. Rammler, 'The Laws Governing the Fineness of Powdered Coal', *Journal of the Institute of Fuel*, vol. 7, pp. 29–36, 1933.

[19] D. Leroy *et al.*, 'Ice Crystal Sizes in High Ice Water Content Clouds. Part II: Statistics of Mass Diameter Percentiles in Tropical Convection Observed during the HAIC/HIWC Project', *Journal of Atmospheric and Oceanic Technology*, vol. 34, pp. 117–136, Jan. 2017.

[20] G. Aouizerate *et al.*, 'Ice Crystals Trajectory Calculations in a Turbofan Engine', presented at the 2018 Atmospheric and Space Environments Conference, Atlanta, GA, USA, 2018.

[21] H. Wadell, 'Volume, Shape and Roundness of Quartz Particles', *The Journal of Geology*, vol. 43, no. 3, pp. 250–280, 1935.

[22] D. Leith, 'Drag on Nonspherical Objects', *Aerosol Science and Technology*, vol. 6, no. 2, pp. 153–161, 1987.

[23] A. Holzer and M. Sommerfeld, 'New simple correlation formula for the drag coefficient of non-spherical particles', *Powder Technology*, vol. 184, pp. 361–365, 2008.

[24] P. Trontin, G. Blanchard, A. Kontogiannis, and P. Villedieu, 'Description and assessment of the new ONERA 2D icing suite IGLOO2D', presented at the 9th AIAA Atmospheric and Space Environments Conference, Denver, CO, USA.

[25] A. Guha, 'Transport and Deposition of Particles in Turbulent and Laminar Flow', *Annual Review of Fluid Mechanics*, vol. 40, pp. 311–341, Jan. 2008.

[26] J. Young and A. Leeming, 'A theory of particle deposition in turbulent pipe flow', *J. Fluid Mech.*, vol. 340, pp. 129–159, 1997.

[27] R. Clift and W. H. Gauvin, 'The motion of particles in turbulent gas streams', *Proceedings Chemeca*, vol. 1, pp. 14–24, 1970.

[28] M. Chrust, G. Bouchet, and J. Dusek, 'Parametric study of the transition in the wake of oblate spheroids and flat cylinders', *J. Fluid Mech.*, vol. 665, pp. 199–208, 2010.

[29] A. Haider and O. Levenspiel, 'Drag Coefficient and Terminal Velocity of Spherical and Nonspherical Particles', 1989.

[30] G. H. Ganser, 'A rational approach to drag prediction of spherical and nonspherical particles', 1993.

[31] R. Rasmussen and H. R. Pruppacher, 'A Wind Tunnel and Theoretical Study of the Melting Behavior of Atmospheric Ice Particles. I: A Wind Tunnel Study of Frozen Drops of Radius

< 500 μm', *Journal of the Atmospheric Sciences*, vol. 39, pp. 152–158, 1982.
[32] R. W. Hyland and A. Wexler, 'Formulations for the thermodynamic properties of dry air from 173.15 K to 473.15 K, and of saturated moist air from 173.15 K to 372.15 K, at pressures to 5 MPa', ASHRAE Transactions, 1983.
[33] T. Hauk, E. Bonaccurso, P. Villedieu, and P. Trontin, 'Theoretical and Experimental Investigation of the Melting Process of Ice Particles', *Journal of Thermophysics and Heat Transfer*, vol. 30, no. 4, pp. 946–954, 2016.
[34] S. Chung, 'Survey of Literature on Convective Heat Transfer Coefficients and Recovery Factors', NASA-CR-138747, Jul. 1973.
[35] C. T. Crowe, J. D. Schwarzkopf, M. Sommerfeld, and Y. Tsuji, *Multiphase Flows with Droplets and Particles*, 2nd ed. 2011.
[36] C. Califf and D. Knezevici, 'Use of a Turbofan Engine to Measure Ice Crystal Cloud Concentration In-Flight', presented at the 50th AIAA/ASME/SAE/ASEE Joint Propulsion Conference, Cleveland, OH, USA, 2014.
[37] AGARD, 'Recommended practices for the assessment of the effects of atmospheric water ingestion on the performance and operability of gas turbine engines'. 1995.
[38] T. Bartkus, P. M. Struk, and J. Tsao, 'Development of a Coupled Air and Particle Thermal Model for Engine Icing Test Facilities', presented at the SAE International Conference on Icing of Aircraft, Engines and Structures, Prague, CZ, 2015.
[39] J. P. Veres, P. C. E. Jorgenson, S. M. Jones, and S. Nili, 'Modeling of a Turbofan Engine With Ice Crystal Ingestion in the NASA Propulsion System Laboratory', presented at the ASME Turbo Expo 2017: Turbomachinery Technical Conference and Exposition, Charlotte, NC, USA, 2017.
[40] A. Bucknell, M. McGilvray, D. R. H. Gillespie, G. Jones, A. Reed, and B. Collier, 'Experimental Studies of Ice Crystal Accretion on an Axisymmetric Body at Engine-Realistic Conditions', presented at the 2018 Atmospheric and Space Environments Conference, Atlanta, GA, USA, 2018.
[41] T. Hauk, I. Roisman, and C. Tropea, 'Investigation of the Impact Behaviour of Ice Particles', *6th AIAA Atmospheric and Space Environments Conference 16-20 June 2014, Atlanta, GA*, 2014.
[42] G. Vidaurre and J. Hallett, 'Particle impact and breakup in aircraft measurement', *Journal of Atmospheric and Oceanic Technology*, vol. 26, no. 5, pp. 972–983, 2008.
[43] P. Guégan *et al.*, 'Critical impact velocity for ice fragmentation', *Journal of Mechanical Engineering Science*, vol. 228, no. 7, 2012.
[44] P. Guégan *et al.*, 'Experimental investigation of the kinematics of post-impact ice fragments', *International Journal of Impact Engineering*, vol. 38, pp. 786–795, 2011.
[45] A. Bucknell, M. McGilvray, and D. R. H. Gillespie, 'A Three-Layer Thermodynamic Model for Ice Crystal Accretion on Warm Surfaces: EMM-C', presented at the International Conference on Icing of Aircraft, Engines, and Structures, Minneapolis, MN, 2019.
[46] D. C. Knezevici, D. M. Fuleki, T. C. Currie, and J. D. MacLeod, 'Particle Size Effects on Ice Crystal Accretion', presented at the 4th AIAA Atmospheric and Space Environments Conference, New Orleans, Louisiana, USA, 2012.
[47] S. T. McClain, M. Vargas, J. Tsao, and A. P. Broeren, 'Ice Roughness and Thickness Evolution on a Business Jet Airfoil', presented at the AIAA Aviation Forum, Atlanta, GA, USA, 2018.
[48] A. Bucknell *et al.*, 'Experimental Study and Analysis of Ice Crystal Accretion on a Gas Turbine Compressor Stator Vane', presented at the International Conference on Icing of Aircraft, Engines, and Structures, Minneapolis, MN, 2019.
[49] P. M. Struk, T. Bartkus, and Tsao J., 'A Method to Interpret Mixed-Phase Measurements using the SEA Multi-Wire Probe in Select Icing Test Facilities', presented at the SAE International 2015 International Conference on Icing of Aircraft, Engines, and Structures, Prague, CZ, Jun-2015.
[50] D. Fuleki, J. L. Chalmers, and B. Galeote, 'Technique for Ice Crystal Particle Size Measurements and Results for the National Research Council of Canada Altitude Ice Crystal Test System', *SAE Technical Paper 2015-01-2125*, 2015.
[51] D. C. Knezevici, D. Fuleki, and J. MacLeod, 'Development and Commissioning of a Linear Compressor Cascade Rig for Ice Crystal Research', *SAE Technical Paper 2011-38-0079*, Jun. 2011.
[52] D. G. Motwani, U. N. Gaitonde, and S. P. Sukhatme, 'Heat Transfer From Rectangular Plates Inclined at Different Angles of Attack and Yaw to an Air Stream', *Journal of Heat Transfer*, vol. 107, pp. 307–312, May 1985.

Nomenclature

Subscripts

0	Total
∞	Freestream
a	Air
acc	Accretion
$conv$	Convection
eq	Equivalent (diameter)
ero	Erosion
$evap$	Evaporation
i	Ice
$imp, stick$	Impinging, sticking (particles)
int	Internal (water)
loc	Local
s, net	Net sticking
sat	Saturation
$sens$	Sensible warming
sub	Sublimation
$subs$	Substrate
$surf$	Surface
t	Timestep t
vap	Vapour
w	Water, wall
x	Axial direction
z	Wall-normal direction

Groups

M	Mach number = $U/\sqrt{\gamma_f R_f T}$
Nu	Nusselt number = HL/k_f
Pr	Prandlt number = $\mu/C_p k_f$
Re	Reynolds number = $\rho UL/\mu_f$
Re_p	Particle Reynolds number = $\rho U_{rel} D_p/\mu_f$
Sc	Schmidt number = $\mu/\rho\, D_{av}$
Sh	Sherwood number = $H_m L/D_{av}$

Latin

a	Spheroid equatorial radius	m
A	Area	m^2
c	Spheroid centre to pole length	m
C	Blade chord	m
C_d	Drag coefficient	-
C_p	Specific heat capacity at constant pressure	J/(kg.K)
$D_{v,xx}$	Diameter for which all particles with $D < D_{v,xx}$ constitute xx% of the total volume	µm
e	Spheroid eccentricity	-
E	Spheroid aspect ratio	-
EMM(-C)	Extended Messinger Model (adapted to ice crystal icing)	
H	Heat transfer coefficient	$W/(m^2.K)$
H_m	Mass transfer coefficient	m/s
$\mathcal{H}$	Erosion model constant	-
$\dot{h}$	Ice growth rate	m/s
J	Chilton-Colburn analogy factor	-
k	Thermal conductivity	W/(m.K)
K_t	Time step multiplication factor	-
$\mathcal{L}$	Kinetic to surface energy fraction	-
L	Characteristic length	m
L_f	Latent heat of fusion	J/kg
L_s	Latent heat of sublimation = $L_f + L_v$	J/kg
L_v	Latent heat of vaporisation	J/kg
$\dot{m}$	Mass flux	$kg/(s.m^2)$
m	Mass	kg
M	Molecular mass	kg/mol
MR	Melt ratio	-
$\dot{n}$	Molar flux	mol/s
P	Pressure	Pa
P_s	Sticking probability	-
PF	Porosity Factor	-
q	Heat flux per unit area	W/m^2
r_f	Recovery factor	-
R_f	Specific gas constant of air	J/(kg.K)
RH	Relative humidity	-
SF	Scale Factor	-
t	Time	s
T	Temperature	K
Twb	Wet bulb temperature	K
T_f	Freezing temperature of water	K
U	Velocity	m/s
V	Volume	m^3
z	Wall-normal distance	m

Greek

β	Collection efficiency	-
γ_f	Isentropic exponent of air	-
Δ	Increment	-
η	Efficiency (stick, erosion)	-
ϵ	Coefficient of restitution	-
μ_f	Dynamic viscosity	Pa .s
ρ	Density	kg/m^3
φ	Sphericity	-
$\varphi_\perp$	Crosswise sphericity	-
τ	Characteristic time (particle, fluid)	-
ω	Vapour mass fraction	-